

# Extending the Dynamic Range of Electronics in a Time Projection Chamber

J. Estee<sup>a,b</sup>, W.G. Lynch<sup>a,b</sup>, R. Wang<sup>j,k</sup>, J. Barney<sup>a,b</sup>, G. Cerizza<sup>a,b</sup>, B. Hong<sup>c</sup>, T. Isobe<sup>d</sup>, G. Jhang<sup>b</sup>, M. Kaneko<sup>e</sup>, M. Kurata-Nishimura<sup>d</sup>, P. Lasko<sup>f</sup>, J. W. Lee<sup>c</sup>, J. Łukasik<sup>f</sup>, A.B. McIntosh<sup>g</sup>, T. Murakami<sup>e</sup>, P. Pawłowski<sup>f</sup>, K. Pelczar<sup>i</sup>, C. Santamaria<sup>b</sup>, D. Suzuki<sup>d</sup>, M. B. Tsang<sup>b</sup>, S.J. Yennello<sup>g</sup>, Y. Zhang<sup>h</sup>, and the S $\pi$ RIT collaboration

<sup>a</sup>*Dept. Physics and Astronomy, Michigan State University, East Lansing, Michigan, 48824, USA*

<sup>b</sup>*National Superconducting Cyclotron Laboratory, East Lansing, Michigan, 48824, USA*

<sup>c</sup>*Department of Physics, Korea University, Seoul 136-703, Republic of Korea*

<sup>d</sup>*RIKEN Nishina Center, Hirosawa 2-1, Wako, Saitama 351-0198, Japan*

<sup>e</sup>*Department of Physics, Kyoto University, Kita-shirakawa, Kyoto 606-8502, Japan*

<sup>f</sup>*Institute of Nuclear Physics PAN, ul. Radzikowskiego 15231-342 Kraków, Poland*

<sup>g</sup>*Dept. of Physics and Astronomy, Texas A&M University, College Station, TX 77843, USA*

<sup>h</sup>*Department of Physics, Tsinghua University, Beijing 100084, P. R. China*

<sup>i</sup>*Faculty of Physics, Astronomy and Applied Computer Science, Jagiellonian University, ul. Gołębia 24, 31-007 Kraków*

<sup>j</sup>*State Key Laboratory of Radiation Medicine and Protection, School of Radiation Medicine and Protection, Soochow University, Suzhou 215123, China*

<sup>k</sup>*Collaborative Innovation Center of Radiological Medicine of Jiangsu Higher Education Institutions, Suzhou 215123, China*

---

## Abstract

When Time Projection Chambers (TPCs) are used in low to intermediate nuclear collisions, the mass and momentum range covered by the emitted particles cover a wide range in energy losses. Many TPC readout electronics currently only have a single gain output with a fixed dynamic range. In a recent set of experiments using the SAMURAI Pion-Reconstruction and Ion-Tracker (S $\pi$ RIT) TPC, it was important to simultaneously measure relativistic pions and heavy ion tracks from the same collisions. As a tracks energy loss is collected and multiplied by the anode wires, a distribution of image charges are induced on the TPC read out pads. If the avalanche on a wire is large enough, the charge collected on a pad will saturate the electronics, though only for pads directly underneath the avalanche; pads further away in the distribution will not be saturated. Using these unsaturated pads and the known distribution function,

we can estimate the saturated pads, increasing the dynamic range by a factor of 10.

*Keywords:* `elsarticle.cls`, L<sup>A</sup>T<sub>E</sub>X, Elsevier, template

*2010 MSC:* 00-01, 99-00

---

## 1. Introduction

Charged particles emitted in low to intermediate energy nuclear collisions cover a large range in energy losses from very small energy losses, for minimum ionizing particles, to much higher energy losses, for slower moving, heavy fragments. Figure 1 shows the range of momenta typically observed in intermediate energy collisions, around 300 MeVA, and the energy loss range involved.

Measuring the full range in energy losses have motivated the development of large dynamic range electronics, which are able to switch between high and low gains covering a very large dynamic range; however, many current Time Projection Chambers (TPCs) readout electronics have a single gain output, presenting a problem for the readout of such devices.

Several techniques have been employed to increase the dynamic range for energy losses in TPCs. In the EOS TPC [1], a larger dynamic range was achieved by lowering the voltage on selected anode wires, decreasing the gas amplification on those wires. In the prototype Active Target TPC (PAT-TPC) an equivalent reduction in gain was achieved by lowering the electronics gain for some of the readout channels. me sections, and optimizing the gain for strongly ionizing particles in others. For strongly ionizing particles, lowering the gain improves the momentum resolution, while worsening the dE/dx resolution, and vice versa for weakly ionizing particles.

These strategies have drawbacks because in many applications the experiment's requirements cannot accept the associated degradation in the dE/dx resolution, or the momentum resolution. Finding the solution to this problem has motivated the development of software based analysis that will extend the dynamical range of TPCs; we illustrate an alternate approach to expand the

dynamic range within the context of a standard multi-wire TPC, without the need of extra hardware or dedicating regions of lower gain.

Many TPC readout electronics have a single gain output with a dynamic range (defined the ratio of the maximum signal to the electronic noise) of no more than 1000:1. In our case the maximum signal to noise was about 700:1. We required the smallest signal of minimum ionizing particles (m.i.p.) to be 20:1, setting the dynamic range to be 35 times m.i.p. Figure 1 illustrates the effect saturation has on the measured momentum of the particles. The shaded region shows where 35 times that of the minimum ionizing pion signal where we could expect saturation to occur. While the pion's momentum range can fully be measured, without saturation effects, heavier particles would be harder to resolve in  $dE/dx$  at lower momentum.

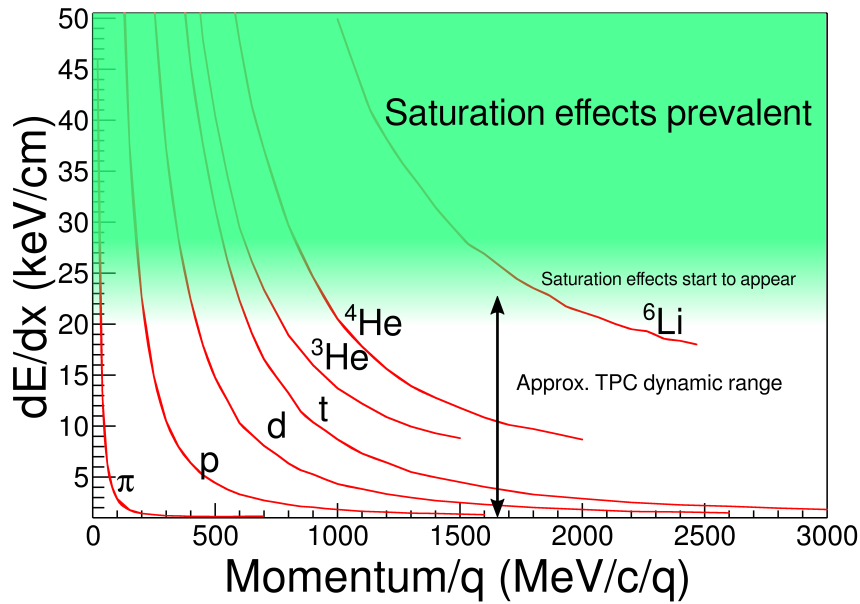


Figure 1:

**1.1 TPC Overview.** We begin our discussion by describing some basic properties of the SAMURAI Pion Reconstruction and Ion-Tracker (S $\pi$ RIT) TPC [2]. For the following discussion we have defined the +x axis to point to the left of the

beam, the  $-y$  axis to point down into the drift volume, and the  $+z$  axis to point along the beam.

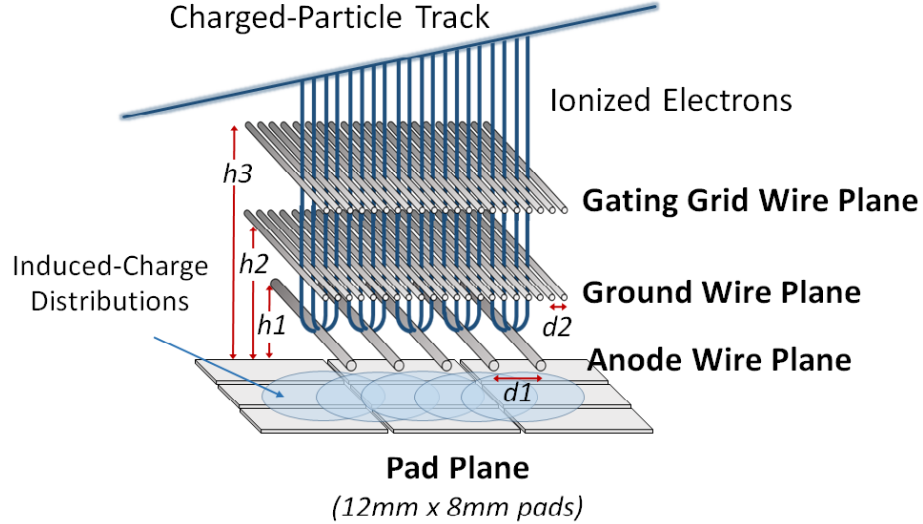


Figure 2: Cartoon graphic showing the 3 wire planes and a section of the pad plane.  $h_3 = 14$  mm,  $h_2 = 8$  mm,  $h_1 = 4$  mm,  $d_2 = 1$  mm,  $d_1 = 4$  mm. This graphic is inverted from the actual wire planes and pad plane to display the perspective easier.

*Pad plane.* The S $\pi$ RIT TPC pad plane is composed of a rectangular charge sensitive pads, each with an x dimension of 8 mm wide, and a z dimension of 12 mm. These pads are arranged in a grid measuring 112 by 108 pads with a total area of 1344 mm x 864 mm.

*Wire planes.* As illustrated in Figure 2, the S $\pi$ RIT TPC consists of three wire planes below the pad plane, with the wires aligned along the x-axis. The wire plane farthest from the pad plane (14 mm) operates as an ion-gate or a gating grid [3]. The middle wire plane (8 mm) is grounded. When the gating grid is open, electrons ionized by reaction products in the drift volume drift through both the gating grid and ground planes.

Closest to the pad plane is the high voltage, anode wire plane (4 mm), consisting of 20  $\mu\text{m}$  diameter wires spaced 4 mm apart. In the vicinity of

55 these wires an avalanche occurs multiplying the secondary electrons drifting up from the drift volume, created from the track's energy loss in the detector gas. When these secondary electrons reach the anode wires, they are amplified on the order of 1000 times creating electron and ion pairs. It is the motion of these slow moving ions, as they drift away from the anode wires, that induces image 60 charges on the read out pads above. The distribution of image charged on the pad plane is centered about the avalanche region on the wires and its width is fixed by the distance from the pad plane.

The anode wires are sectioned off into 14 independent sections, each containing 26 wires; 12 sections were biased to 1460 V. This setting was optimized 65 to ensure m.i.p. particles such as pions would have a signal to noise ratio of around 20:1. The two remaining sections were biased to 1214 V due to high current issues, reducing the gas gain by a factor of 10 times as compared to the other anode sections. As demonstrated by the EoS TPC [1], lowering the anode wires effectively extended the dynamic range. This gain reduction allowed for 70 a direct validation of the success of the new method for extending the dynamic range presented here.

*Generic Electronics for TPCs.* Signals in the S $\pi$ RIT TPC are amplified and digitized by the recently developed Generic Electronics for TPCs (GET) [4]. Short cables transmit the signals from the pads to the inputs of the AGET chips. 75 Each AGET chip services 64 pads (63 pads are connected in our case), contains a pre-amplifier, and a Switched Capacitor Array (SCA), with a maximum of 512 time buckets with an adjustable sampling frequency of 1 to 100 MHz. Four AGET chips are mounted on one AsAd (ASIC and ADC) motherboard. The gain of each AGET can be configured as 0.12, 0.24, 1.0, or 10 pC over the whole 80 dynamic range, and the ADCs on each AsAd board provides 12 bit resolution. The peaking times of the shaping amplifiers can be set to 69, 117, 232, 501, 720, or 1014 ns. In this experiment, the gain was set to the highest setting, 0.12 pC, the peaking time 117 ns, and the sampling frequency 25 MHz (resulting in 40 ns time buckets). The Aget 2.0, asad 2.1, and cobo 1.0 firmware versions

85 were used. The variations in the electronics were calibrated by measuring the response of each channel to a injected reference pulse, covering the full dynamic range of each channel.

Analysis Software. The S $\pi$ RITROOT software is modular tasked based code based on FAIRROOT package written in C++. The tasks in the S $\pi$ RITROOT 90 software reconstruction are:

- Decoder task
- Pulse Shape Algorithm (PSA Task)
- Helix Track Finding Algorithm
- Clustering Algorithm
- 95 • Track Fitting (GENFIT package)
- Vertex Fitting (RAVE package)

The decoder task converts the binary data file into a container class which maps the electronics channels into the corresponding pads and (x,z) coordinates.

100 There may be several pulses in a pad coming from two tracks passing under the same pad separated by arrival time. Using an expected pulse shape the PSA task fits these pulses within a pad, giving the arrival time of the drifted electrons from that track. The height of the pulse is proportional to the total charge of that event, Q. The y-coordinate is calculated as  $y = v \cdot t_0$  where v is the drift velocity and  $t_0$  the arrival time of the pulse. Combining all the 105 information from these first two tasks, (x,y,z,Q), we construct what is called a "hit".

110 The Helix Track Finding Algorithm finds the collection of hits belonging to one track out of all the hits in an event. Hits within a track are then reduced into clusters. A cluster's position is the average position of the hits within a cluster, with the total charge of the cluster being the sum of the hits' charges. A clusters average position represents an estimate of the track's position.

The clusters are then fitted in the GENFIT track fitting package [5], giving the final momentum. A final vertex is fitted from the tracks using the package RAVE [6].

**115** *Definition of clustering.* A brief description of the method of clustering is illustrated in Figure 3. It is impractical to cluster in both x and z-axis and we choose to only cluster the hits along one axis. The clustering direction depends on the angle the track makes with respects to the x-axis, defined as  $\theta$ . For a track going along the z-axis the crossing angle is defined as  $90^\circ$ , and a track going along the **120** x-axis defined as  $0^\circ$ . In the case that the crossing angle is  $45^\circ < \theta \leq 90^\circ$  the clustering direction is along the x-axis. For  $0^\circ < \theta \leq 45^\circ$  it is along the z-axis.

The three clusters at the bottom of Figure 3 are clustered along the x-axis and the upper three are along the z-axis, shown by the bolded pads for one of the clusters. The position along the clustering direction is a weighted mean; **125** calculated by weighting the individual hit's positions by their charges  $q_i$ . The other direction is set to the center of the pad. For example if we are clustering along the x-axis for a cluster, the z-position is set to the center of the pad in the z-direction and vice versa.

Clustering in this way gives us better position resolution for calculating the **130** position of each cluster. You could imagine if we calculated the clusters only along the x-axis for tracks with  $\theta = 0^\circ$  the x-position is not well defined. Thus by switching to the direction most perpendicular to the track we get a better position resolution.

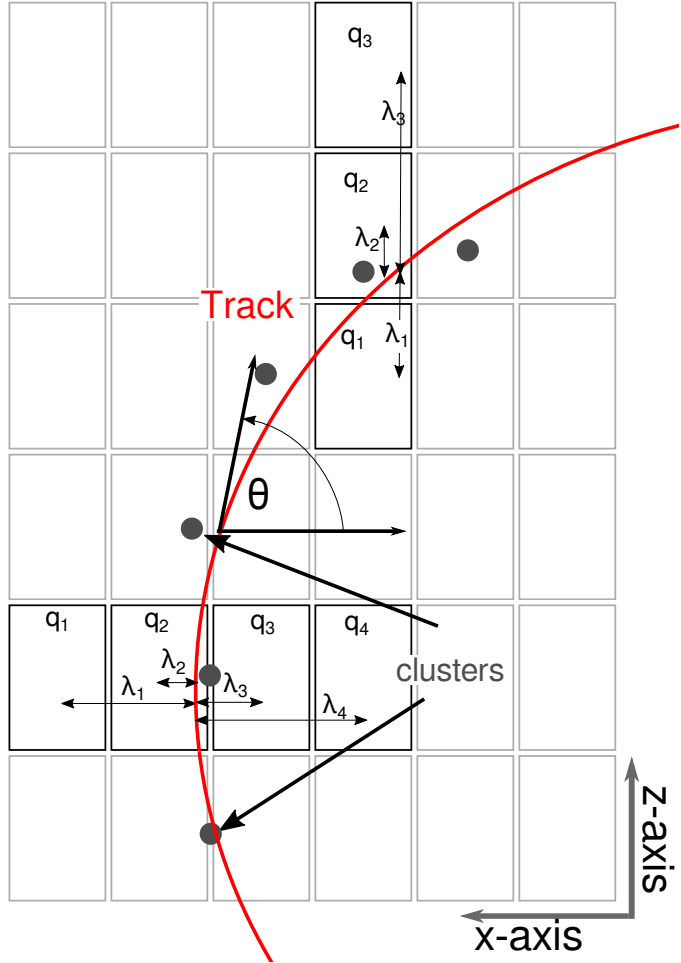


Figure 3: Cartoon graphic of a top down view of a fit to a track passing through several pads. The bolded pads and the charges  $q_i$  represent the hits belonging to that pad and the clusters of the track representing the average position of the track. The three clusters at the bottom are clustered in the x-direction and for the upper three clustered in the z-direction. The estimate of the position of the avalanche is given by the track fit and the position from the center to each pad to the  $\bar{x}$  position is given as  $\lambda_i$ .

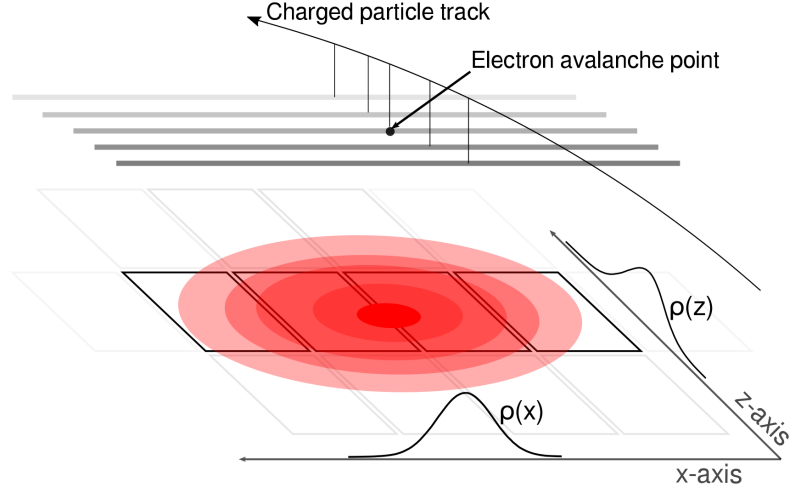


Figure 4: A cartoon illustration of the charge distribution resulting from an electron avalanche on one wire and the projections of the distribution onto the two axis  $\rho(x)$  onto the x-axis and  $\rho(z)$  onto the z-axis. The orientation of the wire planes is flipped upside down to display the perspective better.

## 2. Pad Response Function

135 As illustrated in Figure 4 the distribution resulting from an electron avalanche is 2-dimensional, with the charge observed on each pad being the integral of that distribution over the pad's dimension; also called the Pad Response Function (PRF). The projection onto the x and z-axis of this distribution is shown as  $\rho(x)$  and  $\rho(z)$ .

140 For this particular case the clustering direction would be along the x-axis and is illustrated by the bolded pads; representing the hits resulting from the avalanche. By choosing to clustering only in one direction, we have not included the charge in pads adjacent in the z-axis. While the charge resulting from the tails of  $\rho(z)$  is small our clustering choice has introduced small correlations in  
145 charge between neighboring pads.

*Gatti distribution.* Gatti [7] expressed a semi-empirical equation for the charge distribution in a simple multi-wire TPC such as that found in the S $\pi$ RIT TPC.

Given in Eq. 1, the function depends only on the width of a pad ( $w$ ), height of the anode plane to the pad plane ( $h$ ), and the distance of the pad center to the avalanche point  $\lambda$ . It is a single parameter equation where the two parameters  $K_1 = \frac{K_2\sqrt{K_3}}{4\text{atan}(\sqrt{K_3})}$  and  $K_2 = \frac{\pi}{2} \left(1 - \frac{\sqrt{K_3}}{2}\right)$  depend on the parameter  $K_3$ , which is a function of the ratio of the anode wire diameter to the height of the anode wires to the pad plane.  $K_3$  can be looked up in a graph in [8] and [7].

$$\begin{aligned} PRF_{gatti}(\lambda) &= \frac{K_1}{K_2\sqrt{K_3}} [\arctan(\sqrt{K_3} \tanh[K_2(\frac{\lambda}{h} + \frac{w}{2h})]) \\ &\quad - \arctan(\sqrt{K_3} \tanh[K_2(\frac{\lambda}{h} - \frac{w}{2h})])] \end{aligned} \quad (1)$$

*Experimental PRF.* The correlations we introduced by only clustering along one direction do no play a significant role in the particle identification, but cause deviations from the expected Gatti distribution. Also, analytic PRFs only exist for classical multi-wire TPCs. For these reasons it is useful then to experimentally measure the PRF and fit it with some empirical function, typically a Gaussian, to describe its behavior.

As shown in Figure 3, we postulate that the PRF is only a function of the total charge deposited in a cluster  $Q = \sum_i q_i$  and the difference in position of the center of the  $i^{th}$  pad,  $x_i$ , to the mean position  $\bar{x} = \sum_i x_i q_i / Q$ , called  $\lambda_i = x_i - \bar{x}$ . The PRF is simply defined as the charge fraction of each pad as a function of  $\lambda$ , Equation 2.

$$PRF(\lambda_i) = \frac{q_i(\lambda_i)}{Q} \quad (2)$$

Averaging over many events, the resulting experimental PRF for the S $\pi$ RIT TPC is shown in figure 5. Here we see the deviations from the expected analytic Gatti distribution vs fitting with a Gaussian function with two parameters,  $N_0$  and  $\sigma$  given in 3.

$$PRF_{gaus}(\lambda) = N_0 e^{\frac{-\lambda^2}{2\sigma^2}} \quad (3)$$

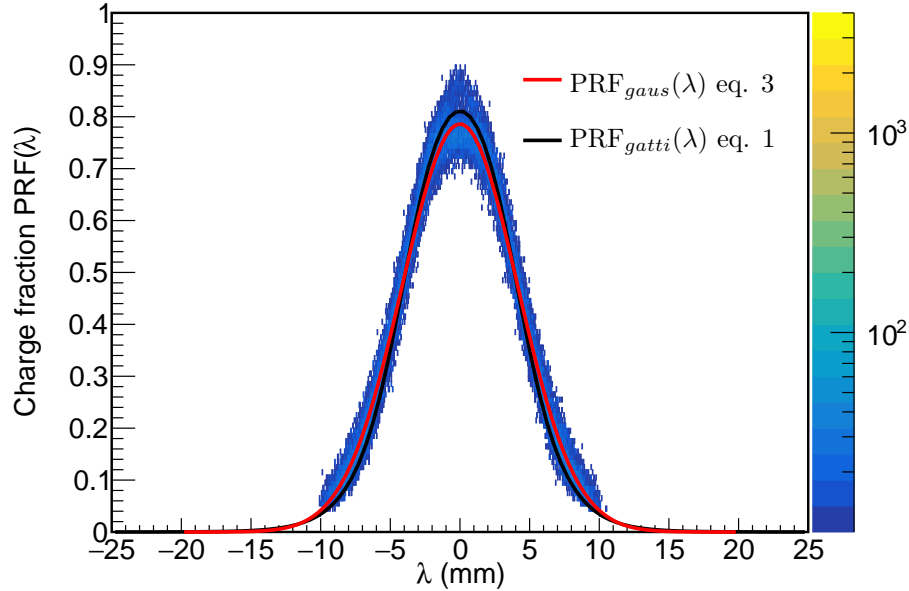


Figure 5: Experimental pad response function of many events for a crossing angle of  $85^\circ < \theta \leq 90^\circ$ .

### 3. PRF vs crossing angle

As mentioned in [7], the shape of the PRF depends on the crossing angle. Plotted in Figure 6 is the PRF of a  $\pi^-$  tracks vs the crossing angle  $\theta$ . One can see the PRF gets wider and wider going from  $90^\circ$  to  $45^\circ$ . This is easily understood as the portion of a track crossing at  $90^\circ$  is at the best position resolution; the PRF gets wider and wider until the PRF at  $0^\circ$  is flat and the position resolution is at it's worst. Since we switch at  $45^\circ$  the clustering direction the opposite trend is seen and the best position resolution is at  $0^\circ$  as the PRF becomes narrower.

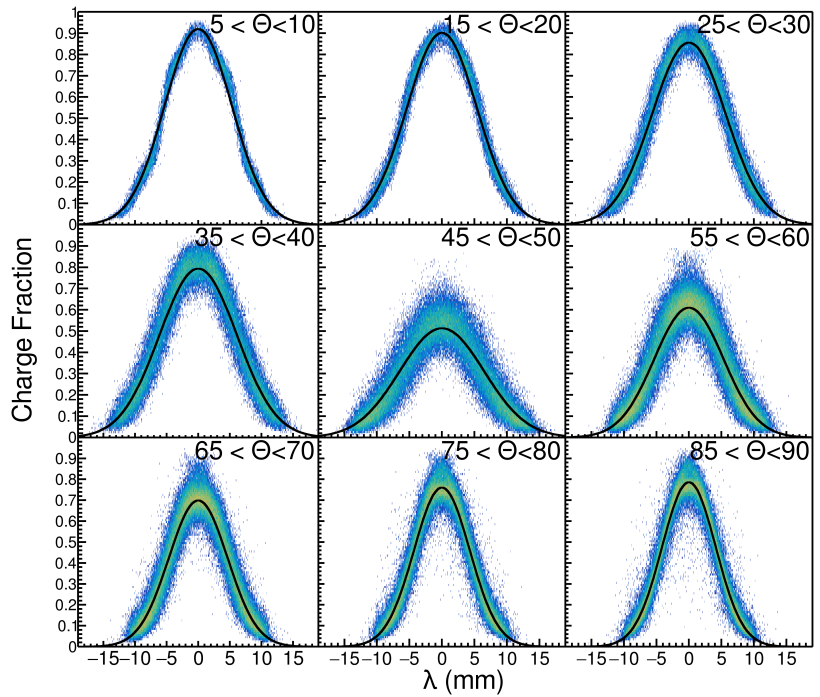


Figure 6: Experimental pad response function as a function of the crossing angle  $\theta$

Coefficient	$c_0$	$c_1$	$c_2$	$c_3$	$c_4$
$0 < \theta < 45$					
$N_0$	.897	5.766E-3	-4.263E-4	7.444E-6	5.705E-8
$\sigma$	5.496	-3.920E-2	2.693E-3	-5.208E-5	5.334E-7
$45 < \theta < 90$					
$N_0$	1.220	-6.258E-2	1.608E-3	-1.492E-5	4.654E-8
$\sigma$	31.368	-1.109	1.779E-2	-1.336E-4	3.940E-7

Table 1: Coefficients of the 4 $th$  order polynomial fit to the Gaussian parameters  $N_0$  and  $\sigma$ . The polynomial form is given as  $c_0 + c_1x + c_2x^2 + c_3x^3 + c_4x^4$

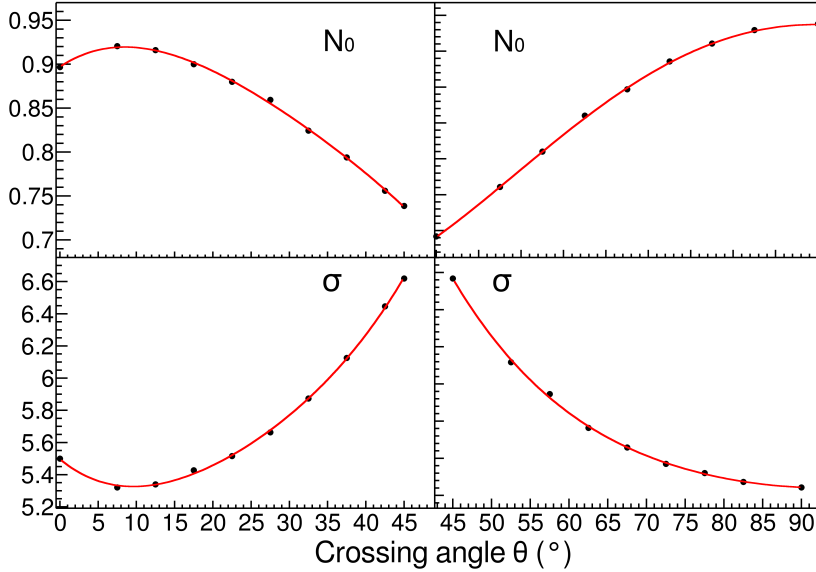


Figure 7: Parameters  $N_0$  and  $\sigma$  as a function of the crossing angle  $\theta$  with the 4 $th$  order polynomial fits given in Table 1.

The Gaussian PRF fitted to the experimental data only has two parameters the normal coefficient and the width, sigma; the mean value is assumed to be 0.  
 180 Fit's were performed to the experimental data by binning 5° from 0° <  $\theta \leq 90^\circ$  and fitting the PRFs. The two variables are plotted vs.  $\theta$  in Figure 7 a 4 $th$  order

polynomial fit between these points allow for  $\theta$  values between points.

*Method of Desaturation.* Figure 8 shows a typical situation of saturated signals. When an avalanche causes a large induced signal, the pad directly underneath collects the largest charge becoming saturated, pads further away experience smaller, non saturating charges;  $q_2'$ ,  $q_3'$  and  $q_1$ ,  $q_4$  respectively as indicated in figure 8.

We will use the term "desaturation" for our process of correcting the charge values of the saturated pads.

The charge deposited on each pad, though saturated, must satisfy the PRF distribution. The small non-saturated tails,  $q_1$  and  $q_4$ , we perform a  $\chi^2$  fit to find the unknown charges of the saturated pads.

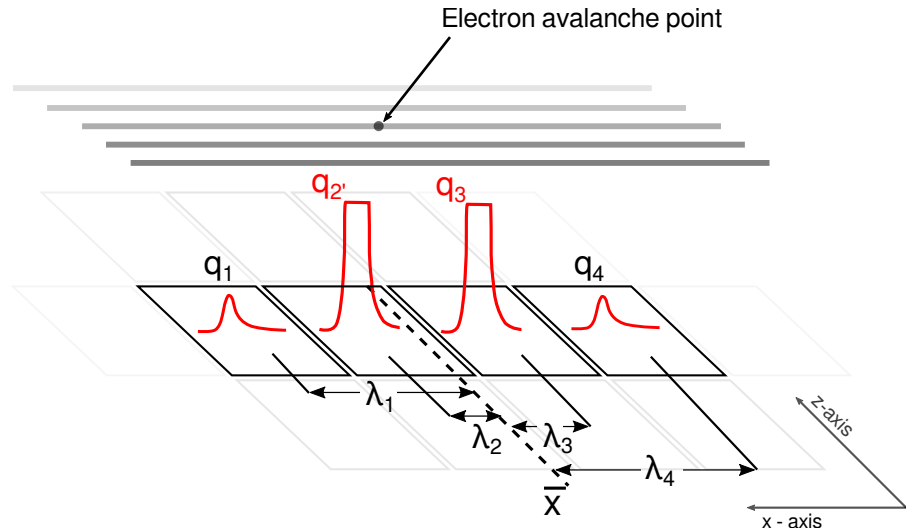


Figure 8: A typical case of a saturating event. The pads directly underneath the avalanche point,  $q_2'$  and  $q_3'$ , are saturated while pads farther away,  $q_1$  and  $q_4$  are not saturated.

#### 4. Experimental data

Two sets of data were used for the testing and validation of this method. A cocktail beam consisting of (p,d,t, ${}^3He$ , ${}^4He$ , ${}^6Li$ , ${}^7Li$ ) light charged particles

was injected into the TPC for calibration purposes, and tuned to two different rigidity,  $\beta\rho$ , settings. The momentum resolution was approximately 1%, as determined by the slits of the BigRIPS fragment separator of the Radioactive Isotope Beam Factory (RIBF) in RIKEN. A thick 21 mm thick aluminum target  
 200 was inserted for part of the lower  $\beta\rho$  setting, further reducing the energy of the beam for a third calibration point.

In a typical cocktail event, one particle enters the TPC volume at a time and parallel to the pad plane; an ideal case for momentum and  $dE/dx$  determination as it does not suffer from inefficiencies of high multiplicity events seen in the  
 205 collision experimental data.

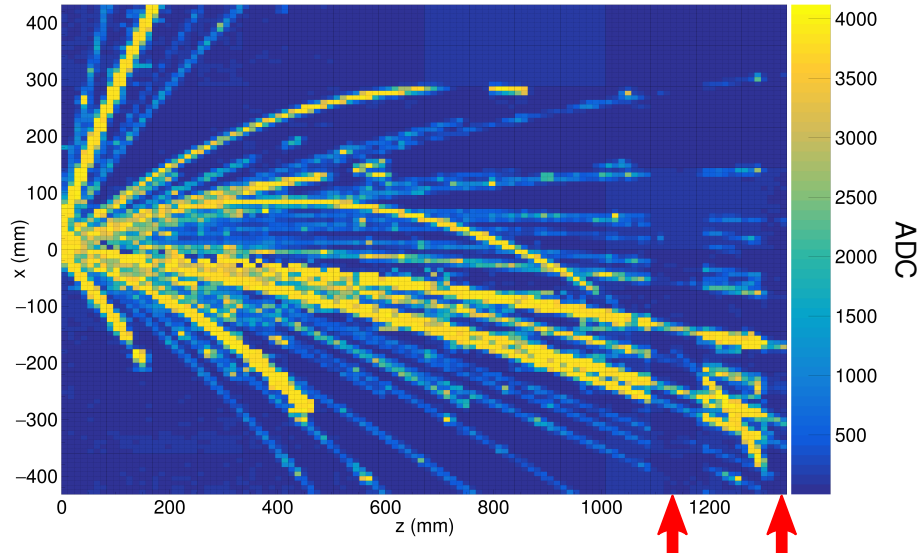


Figure 9: Pad plane projection for a collision event in the TPC. Highlighted by red arrows are two regions of anode wires which had a reduced voltage of 1214 V. The voltage of the rest of the TPC anode wires are 1460 V. The reduction in voltage reduces the gain by a factor of about 10x.

The other type of data was the collision of a  $^{132}\text{Sn}$  beam onto a  $^{124}\text{Sn}$  target triggered on central nuclear collisions. Shown in figure 9 is the typical pad plane response for a central nuclear collision. During the experiment the voltages of two anode sections (as indicated by red arrows in figure 9) were biased to 1214

<sup>210</sup> V. The gain of these sections were also reduced by a factor of about 10 times, as compared with the other sections which were biased to 1460 V. We refer to the 1460 V region as high gain and the 1214 V region as low gain.

## 5. Results

*Low gain vs corrected high gain.* Tracks which saturate pads in the high gain region are not saturated in the low gain region; by comparing the  $dE/dx$  values of these two sections, we can directly measure the success of the high gain region's desaturation using the method described above.

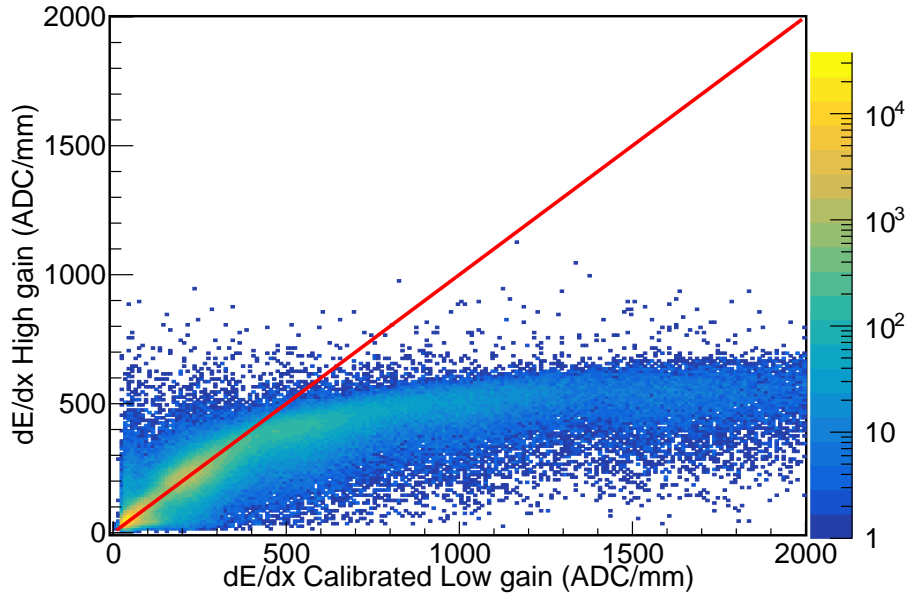


Figure 10: The uncorrected high gain  $dE/dx$  vs low gain  $dE/dx$  collision data.

In figure 10, the effect of saturation can be seen in the high gain region for the uncorrected data. For signals below 400 ADC/mm the electronics are not saturated, and therefore the high and low gain sections agree. The data starts to saturate above 400 ADC/mm in the high gain channels eventually reaching a plateau; the low gain sections have not saturated and provide true  $dE/dx$  values. After applying the desaturation method, the correlation between the high and

low gain sections is restored, as seen in figure 11. We believe the correction to  
225 at least about 2000 ADC/mm, increasing the dynamic range by a factor of 5  
times.

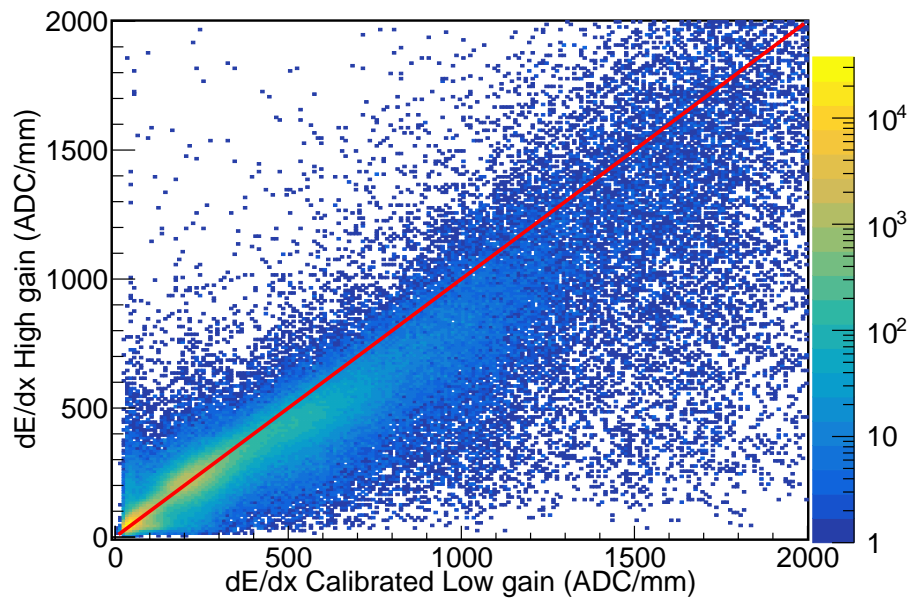


Figure 11: The corrected high gain  $dE/dx$  vs low gain  $dE/dx$  for collision data.

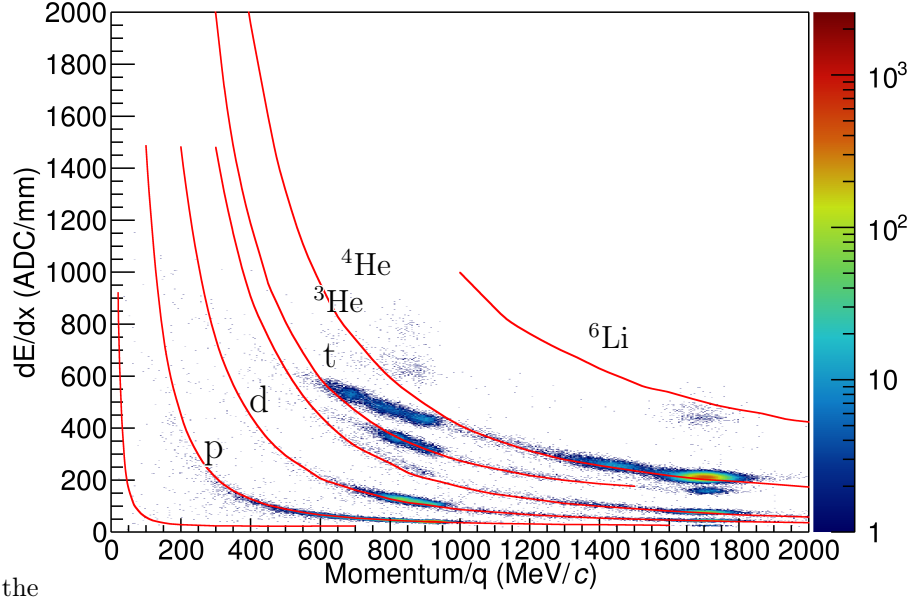


Figure 12: Uncorrected cocktail data.

*Particle Identification (PID).*

$$\frac{ADC}{mm} = 20 \cdot \frac{keV}{cm} \quad (4)$$

Comparing the low to high gain sections provides a direct measurement for determining the success of the desaturation technique, but the goal would be to improve the particle identification (PID). In the following PID plots the red lines represent the most probable energy loss as given by Geant4 straggling functions after calibration to the experimental data, resulting from a linear fit to the uncorrected data, given in equation 4.

There are pronounced PID lines of several particle species in both the uncorrected and corrected cocktail beam PID in figures 12 and 13. Three ovals around 1700 and two near 900 [MeV/c/Z] correspond to the three  $B\rho$  settings injected into the TPC. The tails of the PID lines resulting from the particle losing its initial energy, passing through the walls and other materials outside the main detector volume; therefore lowering their initial momentum.

The uncorrected data in figure 12 shows the effects of saturation; the PID

<sup>240</sup> lines deviate from their theoretical expectations starting around 400 ADC/mm eventually reaching a plateau. After applying the desaturation technique, we see a large improvement; most notably the He and Li particles, which suffer the most from saturation. A more subtle improvement of the lighter particles, (p,d,t), can also be seen in the PID lines at lower momentum.

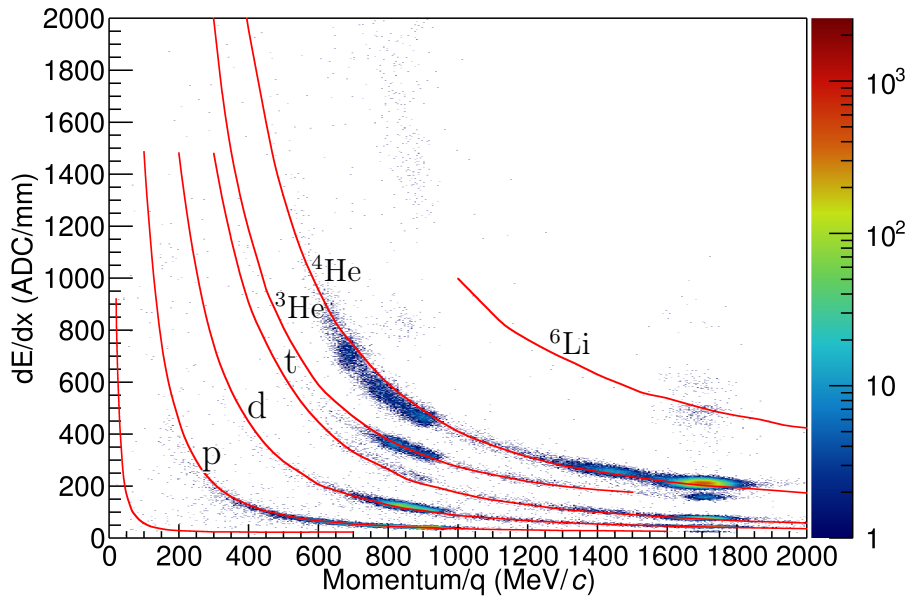


Figure 13: Corrected (desaturated) cocktail data.

<sup>245</sup> Looking at the collision data, in figures 14 and 15, we also see a similar result. Of course the collision data PID suffers from background and inefficiencies than the cocktail beam; nevertheless we can see a similar improvement in the PID lines when comparing the uncorrected to after the desaturation has been applied. Since the separation of particle species at lower momenta and the separation of the Li species into  ${}^6\text{Li}$  and  ${}^7\text{Li}$ , whereas there was little to no separation before.

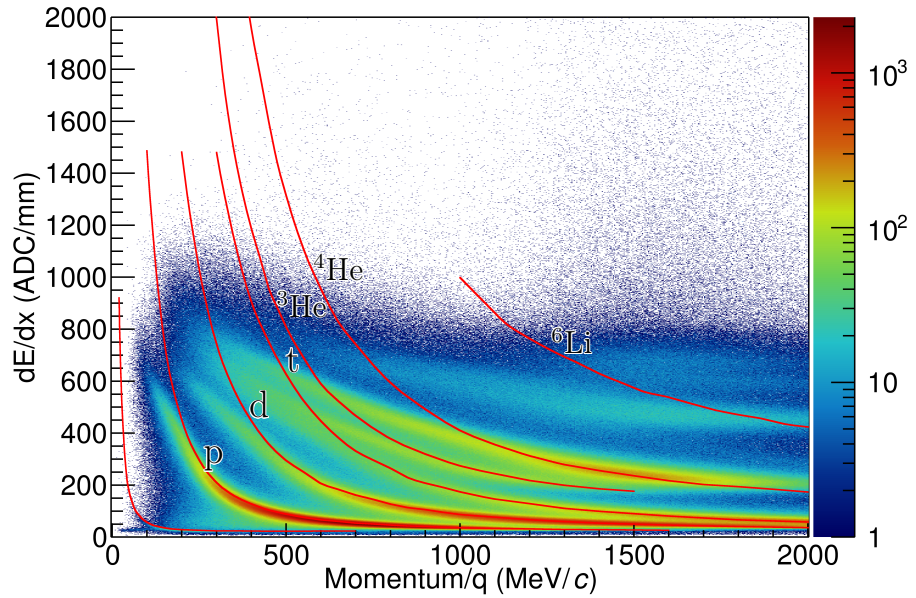


Figure 14: Uncorrected collision data.

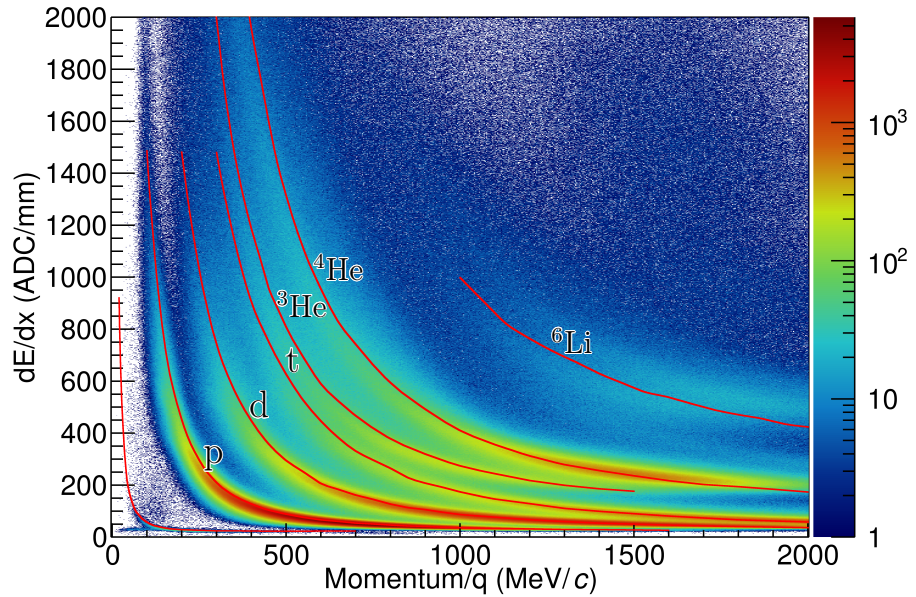


Figure 15: Corrected (desaturated) collision data.

## 6. Conclusion

Saturation reduces  $dE/dx$  resolution and even the maximum charge observable inside of a TPC we have shown that some of the saturation is recoverable. Since the Pad Response Function of the TPC is fixed by the anode wire geometries, an experimental PRF can be calculated from the unsaturated experimental data. The pads resulting from an avalanche on a wire must follow this PRF even if the electronics of some channels directly under the avalanche are saturated, pads further away are not saturated; using these unsaturated pads we perform applying a  $\chi^2$  fit the unknown saturated pads to this PRF function.

Looking at the PID lines, and also making a direct comparison to some low gain sections of the TPC, we were able to extend the dynamic range of our electronics by a factor of about 5 times. This improved PID will allow for us to extend the momentum distributions of all species to lower momenta than what was previously available.

## 7. Acknowledgments

This work was supported by the U.S. Department of Energy under Grant Nos. DE-SC0004835, DE-SC0014530, DE-NA0002923, US National Science Foundation Grant No. PHY-1565546, the Japanese MEXT KAKENHI(Grant-in-Aid for Scientific Research on Innovative Areas) grant No. 24105004, and Polish National Science Center (NCN), under contract Nos. UMO-2013/09/B/ST2/04064 and UMO-2013/10/M/ST2/00624. The computing resources for analyzing the data was provided by the HOKUSAI-GreatWave system at RIKEN.

## References

- [1] G. R. et. al., A tpc detector for the study of high multiplicity heavy ion collisions, IEEE Transactions on Nuclear Science 37 (2) (1990) 56–64. doi: 10.1109/23.106592.

- [2] R. S. et. al., S $\pi$ rit: A time-projection chamber for symmetry-energy studies, NIM A 784 (2015) 513–517. doi:10.1016/j.nima.2015.01.026.
- [3] S. et. al., A gating grid driver for time projection chambers, Nucl. Instr. Meth. Phys. Res. A 853 (2017) 44–52. doi:10.1016/j.nima.2017.02.001.
- [4] E. P. et. al., Get: A generic and comprehensive electronics system for nuclear physics experiments, Physics Procedia 37 (2012) 1799–1804. doi:10.1016/j.phpro.2012.02.506.
- [5] C. H. et. al., A novel generic framework for track fitting in complex detector systems, Nucl. Instrum. Meth. A 620 (2-3) (2010) 518–525. doi:10.1016/j.nima.2010.03.136.
- [6] W. Waltenberger, RaveâĂŹa detector-independent toolkit to reconstruct vertices, IEEE Transactions on Nuclear Science 58 (2) (2011) 434–444. doi:10.1109/TNS.2011.2119492.
- [7] E. G. et. al., Optimum geometry for strip cathodes or grids in mwpc for avalanche localization along the anode wires, Nucl. Instr. Meth. Phys. Res. A 163 (1979) 83–92. doi:10.1016/0029-554X(79)90035-1.
- [8] W. Blum, W. Riegler, L. Rolandi, Particle Detection with Drift Chambers, Springer, Berlin, Heidelberg, 2008.